JOURNAL OF NANOMATERIALS AND APPLICATIONS

Journal of Nanomaterials and Applications

Journal homepage: https://jna.com.vn

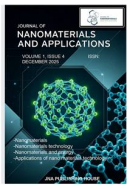

Temperature-Dependent Crystallization, Strain Evolution, and Structural Stability of Chemically Synthesized MoS_2 under Sulfur-Assisted Annealing

Dung Nguyen Trong [1,*], Nguyen Dac Dien [2], Umut Saraç [3]

[1] Faculty of Application Science, University of Transport Technology, 54 Trieu Khuc, Thanh Xuan, 100000, HaNoi, VietNam.

[2] Faculty of Occupational Safety and Health, Vietnam Trade Union University, 169 Tay Son, 100000, HaNoi, VietNam.

[3] Department of Science Education, Bartın University, 74100, Bartın, Türkiye.

Article info

Type of articles:
Original research paper

Corresponding author*:
Dung Nguyen Trong:
dungnt78@utt.edu.vn

Received: 16 August 2026
Revised: 20 September 2026
Accepted: 22 September 2026
Published: 28 September 2026

Abstract: This study investigates the effect of sulfur-assisted N_2 annealing (300, 500, 700, and 900 °C) on chemically synthesized MoS_2 using Raman spectroscopy, XRD, and FE-SEM. Crystallite size increased from 7.2 nm (300 °C) to 13.5 nm (500 °C) and peaked at 22.1 nm (700 °C), accompanied by a strain reduction from 4.8×10^{-3} to 1.2×10^{-3}. At 900°C, crystallite size decreased to 18.4 nm and strain increased to 2.1×10^{-3}, indicating structural deterioration. FE-SEM revealed stacked, flake-like nanostructures with lateral dimensions of 50–100 nm and aggregate thicknesses of 20–30 nm. Annealing at 700 °C provided the optimal balance between crystallite growth and strain relief. The decline at 900 °C is attributed to lattice distortion and potential sulfur non-stoichiometry, establishing a quantitative baseline for thermal processing of MoS_2.

Keywords: MoS_2; thermal annealing; crystallization; Raman spectroscopy; X-ray diffraction; FE-SEM; layered transition-metal dichalcogenide

1. Introduction

Two-dimensional transition-metal dichalcogenides (TMDs) have emerged as pivotal materials for next-generation optoelectronics, catalysis, and energy storage due to their unique thickness-dependent bandgaps, strong spin-orbit coupling, and high surface reactivity [1-5]. Among TMDs, molybdenum disulfide (MoS_2) has been widely investigated for field-effect transistors [6-8], direct-bandgap monolayer photodetectors [9, 10], and electrochemical hydrogen evolution [11-13]. Monolayer MoS_2 exhibits a direct bandgap of $\sim 1.9\ eV$, which transitions to an indirect bandgap of $\sim 1.2\ eV$ in bulk form [9, 14]. Raman spectroscopy serves as a key non-destructive diagnostic tool, where the frequency difference ($\Delta\omega$) between the in-plane E^1_{2g} and out-of-plane A_{1g} modes provides an indirect estimation of layer number [15-19]. Scalable deployment of MoS_2 relies on chemical synthesis methods [20, 21], such as hydrothermal processing [12], sulfurization of molybdenum oxides [22], chemical vapor deposition (CVD) [23–29], and liquid-phase exfoliation [30-33].

Solution-based thermolysis using ammonium tetrathiomolybdate (ATM, $(NH_4)_2MoS_4$) presents a low-cost, high-yield pathway [34-36]. Thermal annealing post-synthesis is indispensable for decomposing residual precursor components, driving atomic rearrangement, and promoting long-range crystallization [37-39]. Although thermal annealing is widely employed to improve the structural ordering of chemically synthesized MoS_2, the relationship between annealing temperature, coherent crystallite growth, lattice strain, and structural deterioration at excessive temperatures remains insufficiently resolved for solution-derived precursor systems. In particular, an increase in diffraction intensity alone does not necessarily provide sufficient evidence of improved structural quality because the observed intensity can also be affected by preferred orientation, sample loading, and measurement conditions. A combined evaluation of diffraction peak position, peak broadening, interlayer spacing, coherent domain size, and lattice strain is therefore necessary to establish a more reliable relationship between thermal processing and structural evolution. Previous studies have extensively investigated MoS_2 synthesis using vapor-phase, hydrothermal, solvothermal, sulfurization, and other chemical routes. However, systematic correlations among coherent crystallite size, interlayer spacing, lattice strain, Raman characteristics, and nanoscale morphology across a controlled annealing-temperature window remain comparatively limited for chemically converted thiomolybdate precursor systems. Furthermore, high-temperature structural deterioration is frequently associated with sulfur loss or sulfur-vacancy formation, although such mechanisms require direct compositional or defect-sensitive evidence. Therefore, distinguishing experimentally established structural changes from proposed defect-chemical mechanisms is essential for developing a scientifically robust thermal-processing strategy. Accordingly, this work systematically investigates the temperature-dependent structural evolution of chemically synthesized MoS_2 under sulfur-assisted inert annealing at 300–900 °C. The specific objectives are to: (i) quantify the evolution of the MoS_2 (002) diffraction peak and coherent crystallite size; (ii) evaluate changes in interlayer spacing and lattice strain as indicators of structural ordering; (iii) correlate XRD-derived structural parameters with Raman

spectroscopy and FE-SEM observations; and (iv) identify the most favorable thermal-processing condition within the investigated temperature range while distinguishing experimentally supported observations from proposed defect-related mechanisms. The principal contribution of this work is a quantitative correlation between annealing temperature, coherent crystallite growth, strain relaxation, and subsequent structural deterioration at excessive temperature in a chemically synthesized MoS_2 system.

2. Experimental Section

2.1. Materials

Ammonium heptamolybdate tetrahydrate ($(NH_4)_6Mo_7O_{24}\cdot 4H_2O$, $\geq 99.0\%$), sodium sulfide nonahydrate ($Na_2S\cdot 9H_2O$, $\geq 98.0\%$), hydrochloric acid (HCl , 37%), sulfur powder (S , 99.99%), absolute ethanol (C_2H_5OH , $\geq 99.8\%$), and deionized water ($18.2\ M\Omega\cdot cm$) were purchased from Sigma-Aldrich and used as received without further purification.

2.2. Preparation of the thiomolybdate precursor

In a typical synthesis, ammonium heptamolybdate tetrahydrate and sodium sulfide nonahydrate were dissolved in deionized water under continuous magnetic stirring at room temperature, maintaining controlled precursor molar ratios (specifically Mo:S = 1:4 for the standard baseline, and 1:1, 1:3, 1:5, 1:7. pH of the solution is adjusted to 4.5 using diluted HCl ($2\ M$), turning the mixture to a characteristic dark red/brown color, indicating the formation of tetrathiomolybdate species (MoS_4^{2-}). The detailed reaction proceeds via acidification as follows:

$$MoS_4^{2-} + 2H^+ \rightarrow MoS_3\downarrow + H_2S\uparrow$$

The mixture was stirred for $2\ h$ at $60\ ^\circ C$. The resulting orange-brown precipitate (MoS_3) was isolated by filtration, washed three times with deionized water and absolute ethanol to remove residual ions (Na^+, Cl^-), and dried under vacuum at $80\ ^\circ C$ for $12\ h$.

2.3. Thermal treatment

The precursor powder ($0.50\ g$) was placed in an alumina boat located at the center of a quartz tube furnace. An auxiliary boat containing $1.00\ g$ of sulfur powder was placed upstream in the low-temperature zone. The tube was purged with high-purity N_2 (99.999%) at $100\ sccm$ for $30\ min$. Under a constant N_2 flow ($50\ sccm$), the furnace was heated at controlled rates (5, 10, 15, and $20\ ^\circ C\ min^{-1}$ for Raman optimization, and fixed at $15\ ^\circ C\ min^{-1}$ for temperature-dependent studies) to target temperatures.

2.4. Characterization

Phase identification and crystallographic parameters were determined by XRD (Bruker D8 Advance, $Cu\ K_\alpha$ radiation, λ=1.5406Å). For XRD measurements, the synthesized powders were dispersed and deposited onto single-crystal Silicon substrates, accounting for the characteristic $Si(311)$ substrate peak

observed in the baseline survey pattern.

Vibrational modes were measured via Raman spectroscopy (Horiba LabRAM HR Evolution, $532\ \mathrm{nm}$ laser excitation at low power $<1\ \mathrm{mW}$). Surface morphology was characterized using FE-SEM (JEOL JSM-7610F operating at $10\ \mathrm{kV}$).

3. Results and Discussion

3.1. Raman characteristics

To evaluate the effect of thermal ramp kinetics on the vibrational properties, Raman spectra were recorded for samples prepared at different heating rates (5--$20\ ^{\circ}\mathrm{C\ min^{-1}}$) while keeping the annealing temperature constant at $700\ ^{\circ}\mathrm{C}$ (Figure 1). All samples exhibit the characteristic E^1_{2g} and A_{1g} modes [40-44]

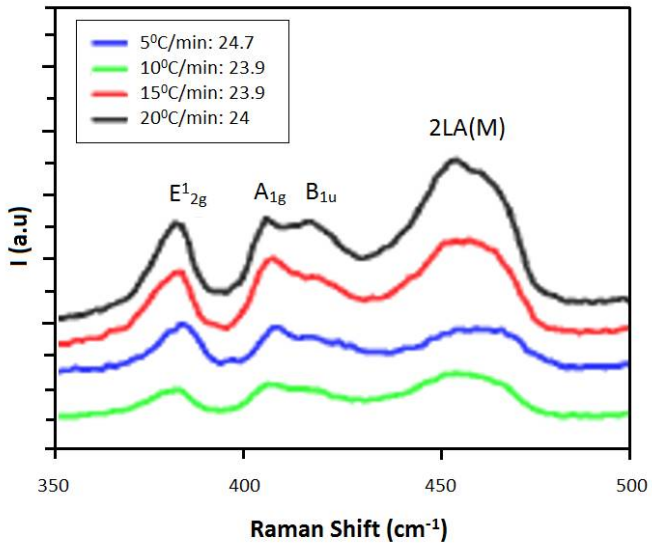

Figure 1. Raman spectra of MoS_2 samples prepared at various heating rates (5, 10, 15, and $20\ ^{\circ}\mathrm{C\ min^{-1}}$) at a fixed annealing temperature of $700\ ^{\circ}\mathrm{C}$.

The legend denotes the corresponding frequency differences ($\Delta\omega$)

3.2. Morphology

The crystallographic refinement and lattice parameters evaluated from XRD profiles are summarized in Table 1. The average coherent domain size (D) along the (002) direction was calculated using Scherrer's equation: $D=\frac{K\lambda}{\beta\cos\theta}$

where $K=0.89$, $\lambda = 0.15418\ \mathrm{nm}$, β is the structural broadening (FWHM in radians), and θ is the Bragg angle. The lattice strain (ε) was calculated using: $\varepsilon=\frac{\beta}{4\tan\theta}$

Table 1. Structural parameters, (002) peak position, interplanar spacing ($d_{(002)}$), FWHM, crystallite size (D), and lattice strain (ε) of MoS_2 annealed at various temperatures.

Annealing Temperature (□C)	Peak Position (002) 2θ (□)	Interplanar Spacing d(002) (Å)	FWHM (002) (□)	Crystallite Size D (nm)	Lattice Strain ε (×10⁻³)
300	14.12	6.27	1.15	7.2	4.8
500	14.28	6.20	0.62	13.5	2.6
700	14.38	6.15	0.38	22.1	1.2
900	14.31	6.18	0.51	**18.4**	**2.1**

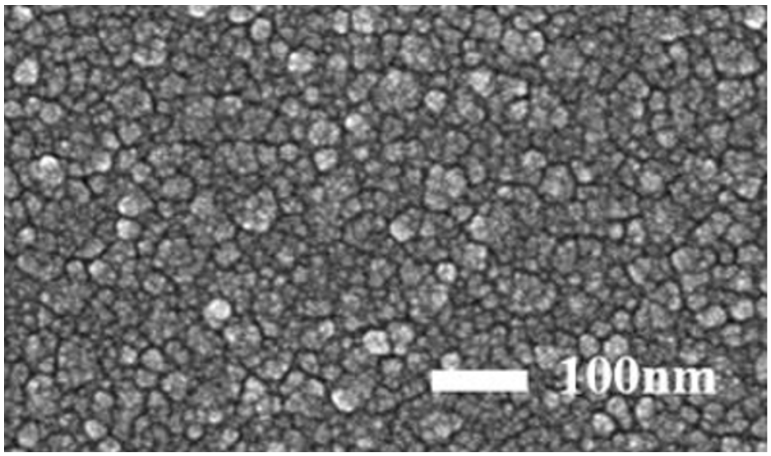

Figure 2. High-resolution FE-SEM morphology showing aggregated flake-like MoS_2 nanostructures synthesized at optimal 700 °C condition.

The interplanar spacing $d_{(002)}$ decreases from 6.27Å at $300\ ^{\circ}\text{C}$ to 6.15Å at $700\ ^{\circ}\text{C}$, approaching the standard theoretical spacing of stoichiometric 2H-MoS_2 (6.15Å, ICDD PDF #96-900-9145). This contraction confirms the removal of residual intercalated species/solvent molecules and tight compression of van der Waals layers. Concurrently, crystallite growth peaks at $22.1\ \text{nm}$ at $700\ ^{\circ}\text{C}$ with a minimum strain of 1.2×10^{-3}.

At $900\ ^{\circ}\text{C}$, the crystallite size decreases to $16.4\ \text{nm}$ while microstrain increases to 1.9×10^{-3}. This reversal is attributed to thermal dissociation and localized sulfur sublimation ($>800\ ^{\circ}\text{C}$), generating sulfur vacancies (V_S) and lattice strain that disrupt long-range stacking order along the c-axis [45-51]. FE-SEM imaging (Figure 2) reveals non-uniform, stacked, flake-like nanostructures with lateral dimensions of $50\text{--}100\ \text{nm}$ and apparent aggregate thickness of $20\text{--}30\ \text{nm}$. The FE-SEM apparent thickness ($20\text{--}30\ \text{nm}$) reflects multi-flake aggregation and edge-curving effects, which aligns consistently with few-layer optical estimations from Raman spectroscopy once mechanical stacking is accounted [52, 53].

3.3. Temperature-dependent XRD evolution

Figures 3–5 display the phase evolution of the synthesized powders. The baseline survey pattern in Figure 3 exhibits a broad background with a distinct peak around $2\theta \approx 56^{\circ}$, corresponding to the $\text{Si}(311)$ plane of the Silicon substrate used during sample deposition. The unannealed sample (Figure 4) displays an

amorphous profile devoid of sharp diffraction peaks from MoS_2. Upon annealing (Figure 5), distinct diffraction peaks emerge at $2\theta \approx 14.4^{\circ}, 32.7^{\circ}, 39.5^{\circ}, 44.2^{\circ}, 49.8^{\circ}, 58.3^{\circ}$, and 60.2°, corresponding to the $(002), (100), (103), (106), (105), (110)$, and (008) planes of hexagonal $2H\text{-}MoS_2$, respectively. At 300$ and $500\ ^{\circ}C$, the (002) feature is broad, indicating limited domain size. The reflection reaches maximum sharpness and intensity at $700\ ^{\circ}C$, confirming optimal long-range crystallization, before suffering intensity attenuation at $900\ ^{\circ}C$ due to thermal strain and sulfur vacancy accumulation [54, 55].

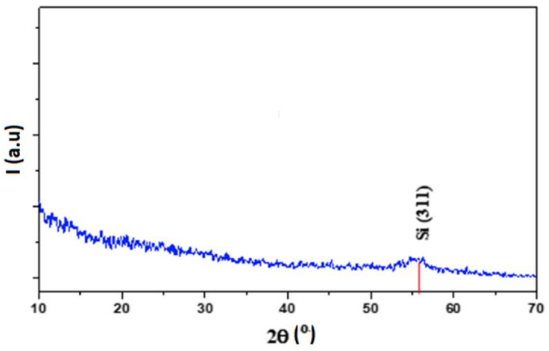

Figure 3. XRD survey pattern of baseline synthesized product.

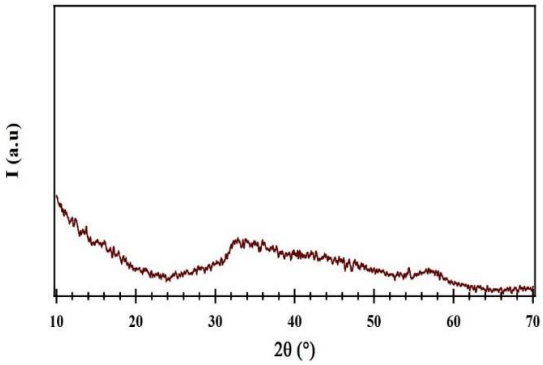

Figure 4: XRD pattern of the unannealed precursor powder showing amorphous nature.

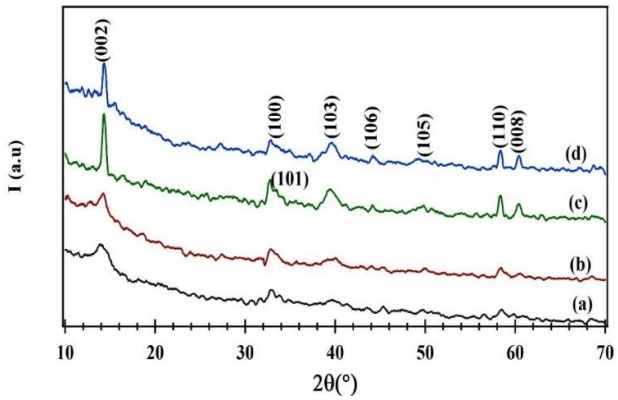

Figure 5. XRD pattern evolution of MoS_2 as a function of annealing temperature: (a) 300 °C, (b) 500 °C, (c) 700 °C, and (d) 900 °C.

3.4. Supporting precursor-ratio experiment

To assess the sensitivity of phase evolution to the starting chemical stoichiometry, a supporting series of MoS_2 powders was prepared by varying the initial molar ratio of ammonium heptamolybdate tetrahydrate to sodium sulfide nonahydrate (1:1, 1:3, 1:5, and 1:7, all annealed at 700 °C for $2\ h$ under $50\ sccm\ N_2$ flow with a heating rate of $15\ ^{\circ}C/min$). Figure 6 and Figure 7 show supporting structural data for varying nominal $AMT : Na_2S$ precursor ratios (1:1, 1:3, 1:5, and 1:7).

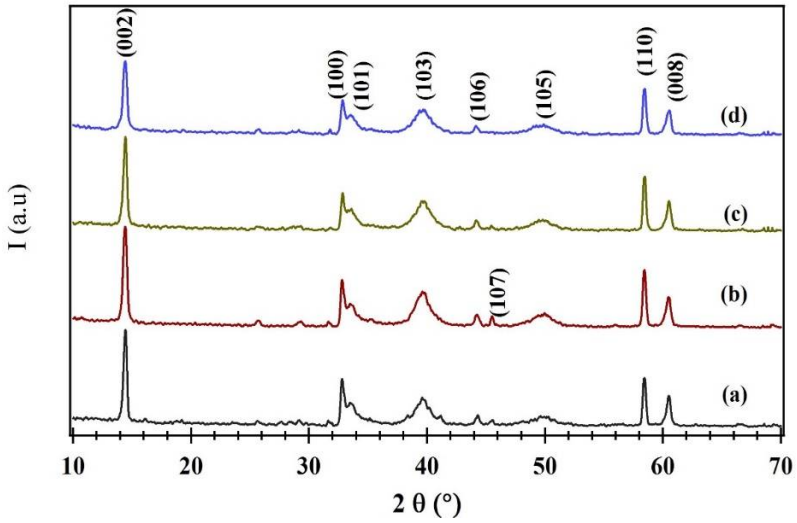

Figure 6: XRD patterns of MoS_2 flakes prepared with different precursor ratios (a) 1:1, (b) 1:3, (c) 1:5, and (d) 1:7 (annealed at 700 °C).

The supplied manuscript also presents XRD and FE-SEM results for nominal AMT:sulfide precursor ratios of 1:1, 1:3, 1:5, and 1:7. These ratios were not adequately defined in the original Methods section. In the revised interpretation, they are treated as a supporting experiment rather than a second primary research question. The authors should explicitly state whether the ratios are molar, mass, or solution-volume ratios and confirm which sulfur reagent was used. All other synthesis and annealing parameters should be stated as constant.

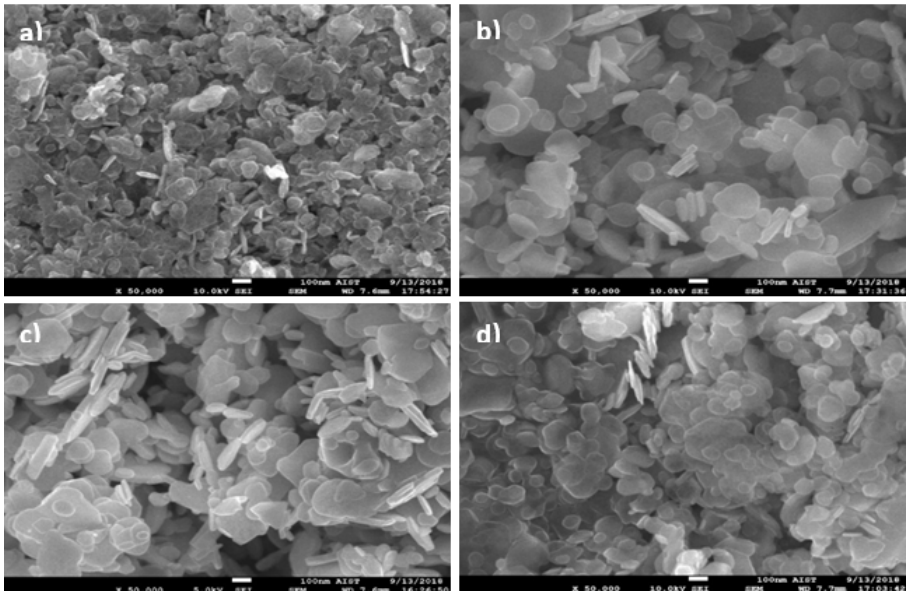

Figure 7. FE-SEM images of MoS_2 powders synthesized with precursor ratios: (a) 1:1, (b) 1:3, (c) 1:5, and (d) 1:7.

The four patterns are reported to be consistent with the hexagonal 2H-MoS_2 phase and dominated by the (002) reflection. The original manuscript observed an additional reflection under some ratios and a decrease in overall diffraction intensity at the highest sulfide ratio. Rather than concluding that precursor ratio has no influence, the evidence supports the narrower statement that no large morphology change was

observed within the investigated ratio window. A broader optimization would require quantitative peak analysis and replication. All precursor ratios yield $2H\text{-}MoS_2$ phase ordering following $700\ ^{\circ}C$ annealing. Higher precursor sulfide ratios (1:5 to 1:7) show minor attenuation in overall XRD peak intensity, indicating that excess sulfur precursor content beyond stoichiometry does not significantly alter the primary flake morphology or crystal phase [12, 22].

3.5. Structure–processing relationship

The comprehensive structural model derived from Raman, XRD, and FE-SEM analyses illustrates a clear three-stage thermal conversion process: Precursor Decomposition ($<300\ ^{\circ}C$): Amorphous thiomolybdate decomposes, releasing volatile products and forming a disordered intermediate matrix [56]. Crystallization & Nucleation ($500\text{--}700\ ^{\circ}C$): Thermally activated atomic diffusion promotes $2H\text{-}MoS_2$ layer nucleation, crystallite expansion ($D = 22.1\ nm$), and lattice strain reduction [37-39]. Thermal Strain & Vacancy Generation ($>700\ ^{\circ}C$): Sulfur loss induces structural microstrain, creating point defects (V_S) and reducing domain coherence along the stacking axis [57, 58].

4. Conclusions

This study demonstrates the critical influence of post-synthesis annealing temperature ($300\text{--}900\ ^{\circ}C$) on the crystallization, strain, and morphology of chemically derived MoS_2 Thermal treatment at $700\ ^{\circ}C$ yields optimal structural quality, characterized by maximum crystallite size ($22.1\ nm$), minimum microstrain (1.2×10^{-3}), and an interplanar spacing ($d_{(002)} = 6.15\text{Å}$) aligned with stoichiometric $2H\text{-}MoS_2$. Annealing at $900\ ^{\circ}C$ introduces lattice strain and decreases structural coherence due to sulfur volatilization. Raman mode separation ($\Delta\omega \approx 23.9\ cm^{-1}$) confirms few-layer structural domains within aggregated $50\text{--}100\ nm$ nanoflakes. These findings establish an optimized processing temperature for scalable chemical preparation of high-quality MoS_2 nanostructures.

Funding: The authors declare that no funds, grants, or other support were received during the preparation of this manuscript.

Data Availability Statement: The data that support the findings of this study are available from the corresponding authors upon reasonable request.

Declaration of competing interest: The authors declare that they have no known competing financial interest or personal relationships that could have appeared to influence the work reported in this paper.

References

[1] X. Huang, Z. Zeng, and H. Zhang, (2013). Metal dichalcogenide nanosheets: Preparation, properties and applications, *Chem. Soc. Rev.*, 42(5), 1934–19461945. https://doi.org/10.1039/C2CS35387C

[2] M. Chhowalla, H. S. Shin, G. Eda, L. J. Li, K. P. Loh, and H. Zhang, (2013). The chemistry of two-dimensional

layered transition metal dichalcogenide nanosheets, *Nat. Chem.*, 5(4), 263–275. https://doi.org/10.1038/nchem.1589

[3] Q. H. Wang, K. Kalantar-Zadeh, A. Kis, J. N. Coleman, and M. S. Strano, (2012). Electronics and optoelectronics of two-dimensional transition metal dichalcogenides, *Nat. Nanotechnol.*, 7(11), 699–712. https://doi.org/10.1038/nnano.2012.193

[4] S. Manzeli, D. Ovchinnikov, D. Pasquier, O. V. Yazyev, and A. Kis, (2017). 2D transition metal dichalcogenides, *Nat. Rev. Mater.*, 2(8), 17033. https://doi.org/10.1038/natrevmats.2017.33

[5] U. Krishnan, M. Kaur, K. Singh, M. Kumar, A. Kumar, (2019). A synoptic review of MoS_2: Synthesis to applications, *Superlattices Microstruct.*, 128, 274–297. https://doi.org/10.1016/j.spmi.2019.02.005

[6] B. Radisavljevic, A. Radenovic, J. Brivio, V. Giacometti, and A. Kis, (2011). Single-layer MoS_2 transistors, *Nat. Nanotechnol.*, 6(3), 147–150. https://doi.org/10.1038/nnano.2010.279

[7] D. Jariwala, V. K. Sangwan, L. J. Lauhon, T. J. Marks, and M. C. Hersam, (2014). Emerging device applications for semiconductor two-dimensional transition metal dichalcogenides, *ACS Nano*, 8(2), 1102–1120. https://doi.org/10.1021/nn500064s

[8] H. Li, Z. Yin, Q. He, H. Li, X. Huang, G. Lu, D. W. H. Fam, A. Y. Tok, Q. Zhang, H. Zhang, (2012). Fabrication of single- and multilayer MoS2 film-based field-effect transistors for sensing NO at room temperature, *Small*, 8(1), 63–67. https://doi.org/10.1002/smll.201101016

[9] K. F. Mak, C. Lee, J. Hone, J. Shan, and T. F. Heinz, (2010). Atomically thin MoS_2: A new direct-gap semiconductor, *Phys. Rev. Lett.*, 105(13), 136805. https://doi.org/10.1103/PhysRevLett.105.136805

[10] A. Splendiani, L. Sun, Y. Zhang, T. Li, J. Kim, C. Y. Chim, G. Galli, and F. Wang, (2010). Emerging photoluminescence in monolayer MoS_2, *Nano Lett.*, 10(4), 1271–1275.
https://doi.org/10.1021/nl903868w

[11] J. Shi, D. Ma, G. F. Han, Y. Zhang, Q. Ji, T. Gao, J. Sun, X. Song, C. Li, Y. Zhang, X.-Y. Lang, Y. Zhang, and Z. Liu, (2014). Controllable growth and transfer of monolayer MoS_2 on Au foils and its potential application in hydrogen evolution reaction, *ACS Nano*, 8(10), 10196–10204. https://doi.org/10.1021/nn503211t

[12] K. Chang and W. Chen, (2011). L-Cysteine-assisted synthesis of layered MoS_2/graphene composites with excellent electrochemical performances for lithium ion batteries, *ACS Nano*, 5(6), 4720–4728. https://doi.org/10.1021/nn200659w

[13] Ronge, E.; Hildebrandt, S.; Grutza, M.-L.; Klein, H.; Kurz, P.; Jooss, C. (2020) Structure of nanocrystalline, partially disordered $MoS_{2+\delta}$ derived from HRTEM An abundant material for efficient HER catalysis. *Catal.*, 10 (8), 856. https://doi.org/10.3390/catal10080856

[14] H. J. Conley, B. Wang, J. I. Ziegler, R. F. Haglund Jr., S. T. Pantelides, and K. I. Bolotin, (2013). Bandgap engineering of strained monolayer and bilayer MoS_2, *Nano Lett.*, 13(8), 3626–3630.
https://doi.org/10.1021/nl4014748

[15] Mitra, S.; Srivastava, D.; Singha, S.S.; Dutta, S.; Satpati, B.; Karppinen, M.; Ghosh, A.; Singha, A. (2020) Tailoring phonon modes of few-layered MoS_2 by in-plane electric field. npj 2D Mater. Appl., 4, 6. https://doi.org/10.1038/s41699-020-0138-y.

[16] Sam, R.T.; Umakoshi, T.; Verma, P. (2020). Probing stacking configurations in a few layered MoS_2 by low frequency Raman spectroscopy. Sci. Rep., 10, 21227.
https://doi.org/10.1038/s41598-020-78238-w.

[17] H. Li, Q. Zhang, C. C. R. Yap, B. K. Tay, T. H. T. Edwin, A. Olivier, and D. Baillargeat, (2012). From bulk to monolayer MoS_2: Evolution of Raman scattering, *Adv. Funct. Mater.*, 22(7), 1385–1390.
https://doi.org/10.1002/adfm.201102111

[18] C. Lee, H. Yan, L. E. Brus, T. F. Heinz, J. Hone, and S. Ryu, (2010). Anomalous lattice vibrations of single- and few-layer MoS_2, *ACS Nano*, 4(5), 2695–2700. https://doi.org/10.1021/nn1003937

[19] A. Berkdemir, H. R. Gutierrez, A. R. Botello-Mendez, N. Perea-Lopez, A. L. Elias, C. I. Chia, B. Wang, V. H. Crespi, F. Lopez-Urias, J. C. Charlier, and H. Terrones, (2013). Identification of individual and few layers of WS_2 using Raman spectroscopy, *Sci. Rep.*, 3(1), 1755. https://doi.org/10.1038/srep01755

[20] M. Chhowalla, H. S. Shin, G. Eda, L.-J. Li, K. P. Loh, and H. Zhang, (2013). The chemistry of two-dimensional layered transition metal dichalcogenide nanosheets, *Nat. Chem.*, 5(4), 263–275.
https://doi.org/10.1038/nchem.1589

[21] X. Huang, C. Tan, Z. Yin, and H. Zhang, (2014). 25th anniversary article: Hybrid nanostructures based on two-dimensional nanomaterials, *Adv. Mater.*, 26(14), 2185–2204.
https://doi.org/10.1002/adma.201304964

[22] Y.-C. Lin, W. Zhang, J.-K. Huang, K.-K. Liu, Y.-H. Lee, C.-T. Liang, C.-W. Chu, and L.-J. Li, (2012). Wafer-scale MoS_2 thin layers prepared by MoO_3 sulfurization, *Nanoscale*, 4(20), 6637–6641.
https://doi.org/10.1039/C2NR31833D

[23] Y. H. Lee, X. Q. Zhang, W. Zhang, M. T. Chang, C.-T. Lin, K.-D. Chang, Y.-C. Yu, J. T.-W. Wang, C.-S. Chang, L.-J. Li, T.-W. Lin, (2012). Synthesis of large-area MoS_2 atomic layers with chemical vapor deposition, *Adv. Mater.*, 24(17), 2320–2325. https://doi.org/10.1002/adma.201104798

[24] K. K. Liu, W. Zhang, Y. H. Lee, Y. C. Lin, M. T. Chang, C. Y. Su, C. S. Chang, H. Li, Y. Shi, H. Zhang, C.-S. Lai, and L. J. Li, (2012). Growth of large-area and highly crystalline MoS_2 thin layers on insulating substrates, *Nano Lett.*, 12(3), 1538–1544. https://doi.org/10.1021/nl2043612

[25] Y. Yu, C. Li, Y. Liu, L. Su, Y. Zhang, and L. Cao, (2013). Controlled scalable synthesis of uniform, high-quality monolayer and few-layer MoS_2 films, *Sci. Rep.*, 3(1), 1866.
https://doi.org/10.1038/srep01866

[26] A. M. van der Zande, P. Y. Huang, D. A. Chenet, T. C. Berkelbach, Y. You, G. H. Lee, T. F. Heinz, D. R. Reichman, D. A. Muller, and J. C. Hone, (2013). Grains and grain boundaries in highly crystalline monolayer molybdenum disulfide, *Nat. Mater.*, 12(6), 554–561. https://doi.org/10.1038/nmat3633

[27] S. Najmaei, Z. Liu, W. Zhou, X. Zou, G. Shi, S. Lei, B. I. Yakobson, J. C. Idrobo, P. M. Ajayan, and J. Lou, (2013). Vapour phase growth and grain boundary structure of molybdenum disulfide atomic layers, *Nat. Mater.*, 12(8), 754–759. https://doi.org/10.1038/nmat3673

[28] X. Ling, Y. H. Lee, Y. Lin, W. Fang, L. Yu, M. S. Dresselhaus, and J. Kong, (2014). Role of the seeding promoter in MoS_2 growth by chemical vapor deposition, *Nano Lett.*, 14(2), 464–472.

https://doi.org/10.1021/nl4033704

[29] Y. Zhan, Z. Liu, S. Najmaei, P. M. Ajayan, and J. Lou, (2012). Large-area vapor-phase growth and characterization of MoS_2 atomic layers on a SiO_2 substrate, *Small*, 8(7), 966–971. https://doi.org/10.1002/smll.201102654

[30] J. Zheng, H. Zhang, S. Dong, Y. Liu, C. T. Nai, H. S. Shin, H. Y. Jeong, B. Liu, and K. P. Loh, (2014). High yield exfoliation of two-dimensional chalcogenides using sodium naphthalenide, *Nat. Commun.*, 5(1), 2995. https://doi.org/10.1038/ncomms3995

[31] X. Fan, P. Xu, D. Zhou, Y. Sun, Y. C. Li, M. A. T. Nguyen, M. Terrones, and T. E. Mallouk, (2015). Fast and efficient preparation of exfoliated 2H MoS_2 nanosheets by sonication-assisted lithium intercalation and infrared laser-induced 1T to 2H phase reversion, *Nano Lett.*, 15(9), 5956–5960. https://doi.org/10.1021/acs.nanolett.5b02091

[32] P. Joensen, R. F. Frindt, and S. R. Morrison, (2008). Single-layer MoS_2, *Mater. Res. Bull.*, 21(4), 457–461. https://doi.org/10.1016/0025-5408(86)90011-5

[33] S. S. Chou, B. Kaehr, J. Kim, B. M. Foley, M. De, P. E. Hopkins, J. Huang, C. J. Brinker, and V. P. Dravid, (2013). Chemically exfoliated MoS_2 as near-infrared photothermal agents, *Angew. Chem. Int. Ed.*, 52(15), 4160–4164. https://doi.org/10.1002/anie.201209229

[34] Desai, P.; Todankar, B.; Ranade, A.K.; Kondo, M.; Dewa, T.; Tanemura, M.; Kalita, G., (2021). Synthesis of MoS_2 Layers on GaN Using Ammonium Tetrathiomolybdate for Heterojunction Device Applications. Cryst. Res. Technol., 56(6), 2000198. https://doi.org/10.1002/crat.202000198

[35] J. Lian, H. Liu, S. Han, J. Lian, (2021). MoS_2 nanosheet-polypyrrole composites deposited on reduced graphene oxide for supercapacitor applications. ACS Appl. Nano Mater., 4, 1330–1339. https://doi.org/10.1021/acsanm.0c02899

[36] H. S. S. R. Matte, A. Gomathi, A. K. Manna, D. J. Late, R. Datta, S. K. Pati, and C. N. R. Rao, (2010). MoS_2 and WS_2 analogues of graphene, *Angew. Chem. Int. Ed.*, 49(24), 4059–4062. https://doi.org/10.1002/anie.201000009

[37] Timpel, M.; Ligorio, G.; Ghiami, A.; et al., (2021). 2D-MoS_2 goes 3D: transferring optoelectronic properties of 2D MoS_2 to a large-area thin film. npj 2D Mater. Appl., 5, 64. https://doi.org/10.1038/s41699-021-00244-x

[38] Kwack, Y.-J.; Can, T.T.T.; Choi, W.-S., (2021). Bottom-up water-based solution synthesis for a large MoS_2 atomic layer for thin-film transistor applications. npj 2D Mater. Appl., 5, 84. https://doi.org/10.1038/s41699-021-00264-7

[39] K.-K. Liu, W. Zhang, Y.-H. Lee, Y.-C. Lin, M.-T. Chang, C.-Y. Su, C.-S. Chang, H. Li, Y. Shi, H. Zhang, C.-S. Lai, and L.-J. Li, (2012). Growth of large-area and highly crystalline MoS_2 thin layers on insulating substrates, *Nano Lett.*, 12(3), 1538–1544. https://doi.org/10.1021/nl2043612

[40] B. Chakraborty, A. Bera, D. V. S. Muthu, S. Bhowmick, U. V. Waghmare, and A. K. Sood, (2012). Symmetry-dependent phonon renormalization in monolayer MoS_2 transistor, *Phys. Rev. B*, 85(16), 161403(R). https://doi.org/10.1103/PhysRevB.85.161403

[41] H. Sahin, S. Tongay, S. Horzum, W. Fan, J. Zhou, J. Li, J. Wu, and F. M. Peeters, (2013). Anomalous Raman spectra and thickness-dependent electronic properties of WSe_2, *Phys. Rev. B*, 87(16), 165409. https://doi.org/10.1103/PhysRevB.87.165409

[42] Y. Zhao, X. Luo, H. Li, J. Zhang, P. T. Araujo, C. K. Gan, J. Wu, H. Zhang, S. Y. Quek, M. S. Dresselhaus, and Q. Xiong, (2013). Interlayer breathing and shear modes in few-layer MoS_2 and WS_2, *Nano Lett.*, 13(3), 1007–1015. https://doi.org/10.1021/nl304169w

[43] M. A. Pimenta, E. del Corro, B. R. Carvalho, C. Fantini, and L. M. Malard, (2015). Comparative study of Raman spectroscopy in graphene and MoS_2-type transition metal dichalcogenides, *Acc. Chem. Res.*, 48(1), 41–47. https://doi.org/10.1021/ar500280m

[44] X. Zhang, Q. H. Tan, J. B. Wu, W. Shi, and P. H. Tan, (2016). Review on the Raman spectroscopy of different types of layered materials, *Nanoscale*, 8(12), 6435–6450. https://doi.org/10.1039/C5NR07205K

[45] S. Baik, Y. Koo, W. Choi (2022), Decreased n-type behavior of monolayer MoS_2 crystals annealed in sulfur atmosphere. Curr. Appl. Phys., 42, 38–42. https://doi.org/10.1016/j.cap.2022.07.011.

[46] J. Hong, Z. Hu, M. Probert, K. Li, D. Lv, X. Yang, L. Gu, N. Mao, Q. Feng, L. Xie, J. Zhang et. al. (2015). Exploring atomic defects in molybdenum disulfide monolayers, *Nat. Commun.*, 6(1), 6293. https://doi.org/10.1038/ncomms7293

[47] W. Zhou, X. Zou, S. Najmaei, Z. Liu, Y. Shi, J. Kong, J. Lou, P. M. Ajayan, B. I. Yakobson, and J. C. Idrobo, (2013). Intrinsic structural defects in monolayer molybdenum disulfide, *Nano Lett.*, 13(6), 2615–2622. https://doi.org/10.1021/nl4007479

[48] S. Kc, R. C. Longo, R. Addou, R. M. Wallace, and K. Cho, (2014). Impact of intrinsic atomic defects on the electronic structure of MoS_2 monolayers, *Nanotechnol.*, 25(37), 375703. https://doi.org/10.1088/0957-4484/25/37/375703

[49]. Lee, J.; Kim, M.J.; Jeong, B.G.; Kwon, C.; Cha, Y.; Choi, S.H.; Kim, K.K.; Jeong, M.S. (2023), Electrical role of sulfur vacancies in MoS_2: Transient current approach. *Appl. Surf. Sci.,* 613, 155900. https://doi.org/10.1016/j.apsusc.2022.155900.

[50] D. H. Keum, S. Cho, J. H. Kim, D. H. Choe, H. J. Sung, M. Kan, H. Kang, J. Y. Hwang, S. W. Kim, H. Yang, K. J. Chang, Y. H. Lee (2015). Bandgap opening in few-layered monoclinic $MoTe_2$, *Nat. Phys.*, 11(6), 482–486. https://doi.org/10.1038/nphys3314

[51] Y. Koo, W. Choi, (2023). Effects of forming gas annealing on the doping of monolayer MoS_2 crystals. *Curr. Appl. Phys.,* 48, 29–33. https://doi.org/10.1016/j.cap.2023.01.005.

[52] C. Muratore, J. J. Hu, B. Wang, M. A. Haque, J. E. Bultman, M. L. Jespersen, P. J. Shamberger, M. E. McConney, R. D. Naguy, and A. A. Voevodin, (2014). Continuous ultra-thin MoS_2 films grown by low-temperature physical vapor deposition, *Appl. Phys. Lett.*, 104(26), 261604. https://doi.org/10.1063/1.4885391

[53] Ştefan Ţălu, Vu Van Thu, Nguyen Dac Dien, (2026), A state of the art review on MoS_2 preparations and applications, Journal of Nanomaterials and Applications, 2(2), 1-15, https://doi.org/10.65273/hhit.jna.2026.2.2.028

[54] Z. Lin, B. R. Carvalho, E. Kahn, R. Rao, H. Torrones, M. A. Pimenta, and M. Terrones, (2016). Defect engineering of two-dimensional transition metal dichalcogenides, *2D Mater.*, 3(2), 022002. https://doi.org/10.1088/2053-1583/3/2/022002

[55] H. Nan, Z. Wang, W. Wang, Z. Liang, Y. Lu, Q. Chen, D. He, P. Tan, F. Miao, X. Wang, J. Wang, and Z. Ni, (2014). Strong photoluminescence enhancement of MoS_2 monolayer by defect engineering, *ACS Nano*, 8(6), 5738–5745. https://doi.org/10.1021/nn500581q

[56] S. J. Yun, S. H. Chae, H. Kim, J. C. Park, J.-H. Park, G. H. Han, J. S. Lee, S. M. Kim, H. M. Oh, J. Seok, M. S. Jeong, K. K. Kim, and Y. H. Lee, (2015). Synthesis of centimeter-scale monolayer tungsten disulfide film on gold foils, *ACS Nano*, 9(5), 5510–5519. https://doi.org/10.1021/acsnano.5b01529

[57] Y. C. Lin, D. O. Dumcenco, Y. S. Huang, and K. Suenaga, (2014). Atomic mechanism of the semiconductor-to-metal phase transition in single-layer MoS_2, *Nat. Nanotechnol.*, 9(5), 391–396. https://doi.org/10.1038/nnano.2014.64

[58] Ştefan Ţălu, Dung Nguyen Trong, Umut Sarac, Luong Viet Trung, Mai Ho Thi Thanh, Huong Vuong Thi, (2024), Impact of MoS2 Layer Thickness and Donor Concentration on Saturation Current in 4-Layer MOSFET: A Comsol Simulation, Journal of Science and Transport Technology, 4(4), 19-29, https://doi.org/10.58845/jstt.utt.2024.en.4.4.19-29